

Research Article

Time-Domain Topological Energy Imaging Method of Concrete Cavity Defect by Lamb Wave

Wen-Fa Zhu^{1,2}, Wei Shao,¹ Le-Le Peng,¹ Guo-Peng Fan,¹ Xing-Jie Chen,¹ Shu-Bin Zheng,¹ and Hai-Yan Zhang³

¹School of Urban Rail Transportation, Shanghai University of Engineering Science, Shanghai 201620, China

²School of Mechanical and Power Engineering, East China University of Science and Technology, Shanghai 200237, China

³School of Communication and Information Engineering, Shanghai University, Shanghai 200444, China

Correspondence should be addressed to Wen-Fa Zhu; zhuwenfa1986@163.com

Received 5 June 2019; Revised 10 November 2019; Accepted 3 December 2019; Published 20 December 2019

Academic Editor: Mahdi Mohammadpour

Copyright © 2019 Wen-Fa Zhu et al. This is an open access article distributed under the Creative Commons Attribution License, which permits unrestricted use, distribution, and reproduction in any medium, provided the original work is properly cited.

This paper presents an ultrasonic Lamb wave imaging method based on time-domain topological energy to address artifacts in the results of traditional ultrasound imaging methods. This method is based on topological theory and the calculation of the direct and adjoint sound fields in a defect-free reference medium. It focuses the direct and adjoint sound fields at the cavity defect using time reversal and their time-domain topological energy as the pixel values of the image to reduce the artifacts. The physical mechanism of time-domain topological energy (TDTE) imaging is revealed by finite element simulation and experiment. The feasibility of this method for multilayer concrete cavity defect imaging is verified. Compared with the traditional synthetic aperture focusing technique (SAFT) imaging method, the numerical simulation and experimental results show that the method can overcome the influence of ultrasonic Lamb wave dispersion and locate cavity defects with high accuracy and few artifacts. These features indicate the potential of the method in imaging damage concrete structures.

1. Introduction

Concrete is the most widely used material in highway, high-speed railway, and other traffic engineering structures. However, its internal damage is substantially increased because of the influence of dynamic load, environmental temperature, and other factors. The internal damages of concrete, such as cavity defect, seriously affect vehicle speed and safety [1–3]. Therefore, the effective characterization of the degree and scope of concrete cavity is an urgent problem for researchers.

Ultrasound imaging has widely been used in the detection of concrete structural defects such as bridge deck [4–6], concrete column [7], pavement [8, 9], and tunnel [10]. Existing detection methods often use ultrasonic body waves. Concrete is assumed as a homogeneous medium with a single constant shear wave velocity; thus, synthetic aperture focusing technology (SAFT) is used to image concrete structures (such as MIRA [11], EyeCon [11], and Pundit

[12]). However, this assumption only applies to single-layer concrete structures, which limits the application of existing technology in multilayer concrete structures. The difference in acoustic impedance between layers cannot be neglected in cavity defects in highways and high-speed rail structures [13, 14]. In this case, the assumption of a single constant shear wave velocity will inevitably lead to detection errors. Recent advances in SAFT methods (e.g., [15–18]) have theoretically realized the ultrasonic imaging of multilayer concrete structures. However, the detection efficiency of the ultrasonic body wave is low, and meeting the demand of concrete structure in service is difficult [19, 20]. The ultrasonic Lamb wave method, with the advantages of long distance and wide range detection, improves the detection efficiency. However, the echo signal generated by the main lobe pointing to the strong reflective medium on both sides interferes with the incident signal along the main lobe due to the influence of Lamb wave dispersion [21], multimode characteristics, and boundary reflection effect. Moreover,

additional artifacts are retrieved in the defective image by the classical imaging method. The details of defects are closely related to scattering. If the scattering and mode conversion characteristics of defects are not considered in the imaging process, then the detailed feature information of defects is difficult to obtain [22–24]. Therefore, the topological imaging method that completely considers the defect scattering characteristics in the defect reconstruction and imaging process is attracting research attention [25].

Topological imaging originated from shape optimization in the mathematical field. Defect images can be obtained without assuming the location and shape of defects in advance by using the idea of topological asymptotic, which has been successfully applied in ultrasonic body wave imaging [26–28]. The study of topological imaging methods for Lamb wave detection began in the last 10 years. In 2014, Rodriguez et al. [29] successfully realized ultrasonic Lamb wave imaging of a single through-hole defect using topological imaging. In 2017, Lubeigt et al. [30] studied the application of topographic imaging in nondestructive testing of bounded elastic media. The results of weld seam inspection show that the defect characteristics of the reference samples are obvious and the imaging quality is high. Concrete cavity defect is a common form of damage in civil engineering structures. However, research on cavity defects in multilayer structures is inadequate. This study establishes a finite element model and constructs an experimental system to stimulate the generation of ultrasonic Lamb waves in concrete and obtain ultrasonic scattering signals. The time-domain topological energy method is used to realize the accurate imaging of concrete cavity defects, and the method is compared with the traditional SAFT method. The numerical simulation and experimental results consistently show that the time-domain topology energy has high positioning accuracy and few artifacts.

2. Principles of Topological Imaging

The main idea of topological energy imaging in the time domain is to transform the topological progressive process into direct and adjoint problems, that is, direct and adjoint sound fields. The sample containing the scatterer (defect) is called the plate to be tested Ω_m , as shown in Figure 1(a). The test plate whose attribute is completely the same without the scatterer is called the reference test plate Ω_0 , as shown in Figure 1(b). If the excitation signal $x_n(t)$ is applied at the n th element of the linear array and received at each point in the imaging region of the reference plate, then the sound field of the entire imaging region can be obtained through calculation, which is called the direct sound field $U(x, y, t)$.

In the process of sound field calculation, t_ω is set as the cutoff time of the received signal, which should be greater than the time of the received signal at the farthest target point in the imaging region. T_p is the time for the excitation signal to reach the target point $p(x, y)$ in the imaging region. In the Lamb wave propagation model, the point source excitation with $x_n(t)$ as a time function propagates for a certain distance d , and then the signal waveform can be obtained as follows:

$$D_{cp}\{x_n(t); T\} = F^{-1}\left\{F\{x_n(t)\}\exp\left(\frac{i2\pi fd}{c_p}\right)\right\}, \quad (1)$$

where T is the propagation time, $F\{\cdot\}$ is the Fourier transform, $F^{-1}\{\cdot\}$ is the inverse Fourier transform, and c_p is the phase velocity.

According to equation (1), the direct sound field in the imaging region of the reference sample is $U(x, y, t)$:

$$U(x, y, t) = D_{cp}\{x_n(t); t_p\}. \quad (2)$$

The excitation position is unchanged, and the test plate is changed from the reference test plate Ω_0 to the plate to be tested Ω_m . The received signal of the block to be tested at the target point is different from the signal received at the same point in the reference sample, as it was scattered by defects. After the scatter signal is windowed and time-reversed, it is used as a secondary excitation source and reexcited in the reference test plate and then received at each point in the imaging area of the reference test plate. The sound field is called the adjoint sound field $V(x, y, t)$. According to the propagation model of the Lamb wave, the adjoint sound field $V(x, y, t)$ in the reference plate can also be obtained:

$$V(x, y, t) = D_{cp}\{z_0(t); t_\omega - t_p\}, \quad (3)$$

where t_ω is the time at which the scatter signal reaches the last sensor, t_p is the time when the excitation signal reaches the defect, and $z_0(t)$ is the secondary excitation signal.

The imaging function of the TDTE method is not about summing the amplitude of the signal in the time domain but the topological energy value. The absolute values of direct sound field $U(x, y, t)$ and of adjoint sound field $V(x, y, t)$ are taken first, squared, and finally multiplied in order to obtain, after integrating time, the time-domain topology energy value. The topological energy expression in the time domain is

$$G(x, y) = \int_0^T \|U(x, y, t)\|^2 \|V(x, y, t)\|^2 dt, \quad (4)$$

where T is the cutoff time of the signal and point (x, y) is the coordinate of the imaging area.

If the topological energy value of each point is mapped individually with the pixel value of that point, then the topological energy imaging result of the whole time domain can be obtained. It should be noted that the topological energy value of the defect's position is much higher than that of other position.

3. Finite Element Simulation

A commercial software package called PZFlex is used to create the finite element model, which is shown in Figure 2. PZFlex is the time-domain finite element method (FEM). The complex acoustic wave propagation in a three-dimensional model can be simulated by using this method. The upper and bottom surfaces of the model are free, while the remaining four sides are absorbing. The sample is a two-layer concrete bonding structure. The size of the first layer is $1000 \times 1000 \times 50 \text{ mm}^3$, and the physical parameters are as

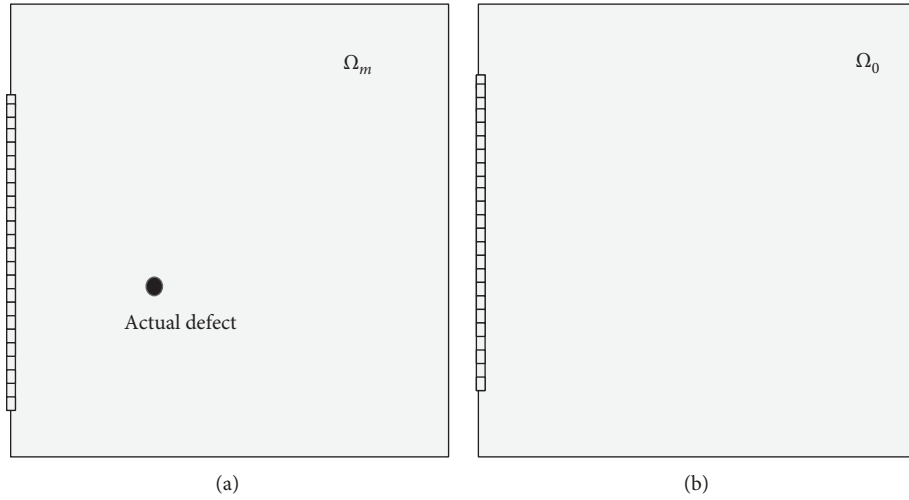


FIGURE 1: Top view of the test plate model: (a) reference test plate; (b) plate to be tested.

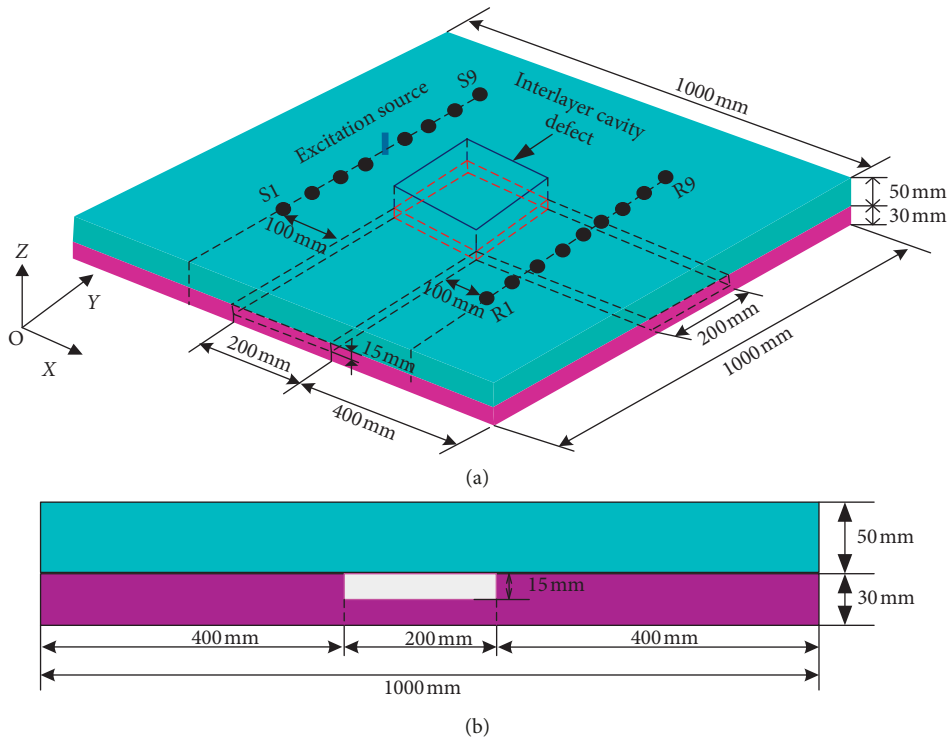


FIGURE 2: Schematic of the finite element model: (a) 3D finite element model; (b) sectional view.

follows: density is 2500 kg/m^3 , longitudinal wave velocity is 4700 m/s , and shear wave velocity is 3100 m/s . The size of the second layer is $1000 \times 1000 \times 30 \text{ mm}^3$, and the physical parameters are as follows: density is 1800 kg/m^3 , longitudinal wave velocity is 2484 m/s , and shear wave velocity is 1521 m/s . A cavity defect having a size of $200 \times 200 \times 15 \text{ mm}^3$ is disposed between the first layer and the second layer of the sample to be inspected. Exciting and receiving sensors are disposed on both sides of the cavity defect. The exciting sensor has nine positions. The position numbers are

sequentially labeled as S1–S9 with an interval of 60 mm . The S1 coordinates are $(300 \text{ mm}, 260 \text{ mm})$, whereas S9 coordinates are $(300 \text{ mm}, 740 \text{ mm})$, and the sensor diameter is 10 mm . The receiving sensor has nine positions, and the position numbers are sequentially labeled as R1–R9 with an interval of 60 mm . The R1 coordinates are $(700 \text{ mm}, 260 \text{ mm})$, whereas the R9 coordinates are $(700 \text{ mm}, 740 \text{ mm})$, and the sensor diameter is 10 mm . The imaging area is located at the center of the model and is $600 \times 600 \text{ mm}^2$ in size.

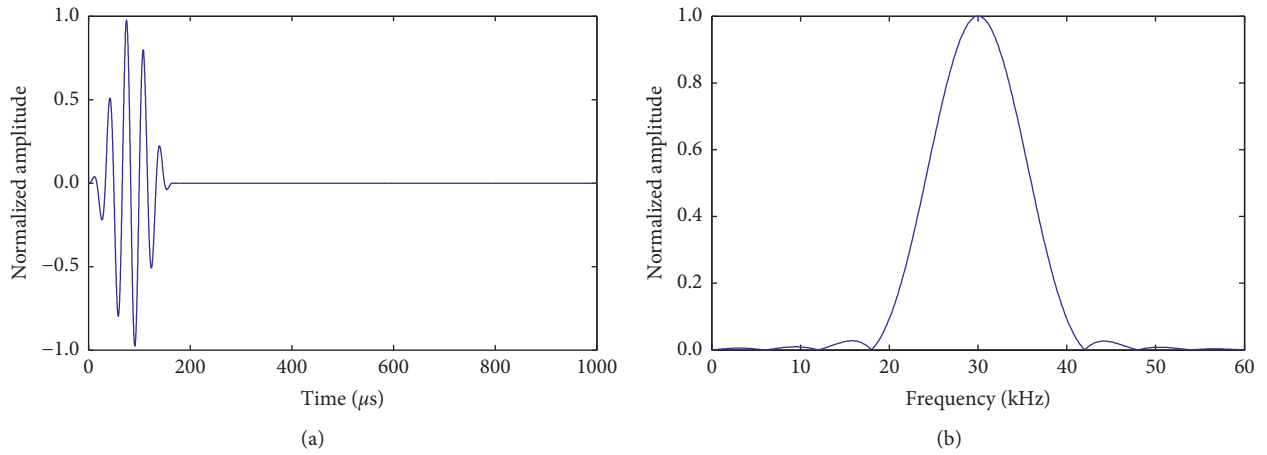


FIGURE 3: Excitation signal time-domain waveform (a) and spectrum (b).

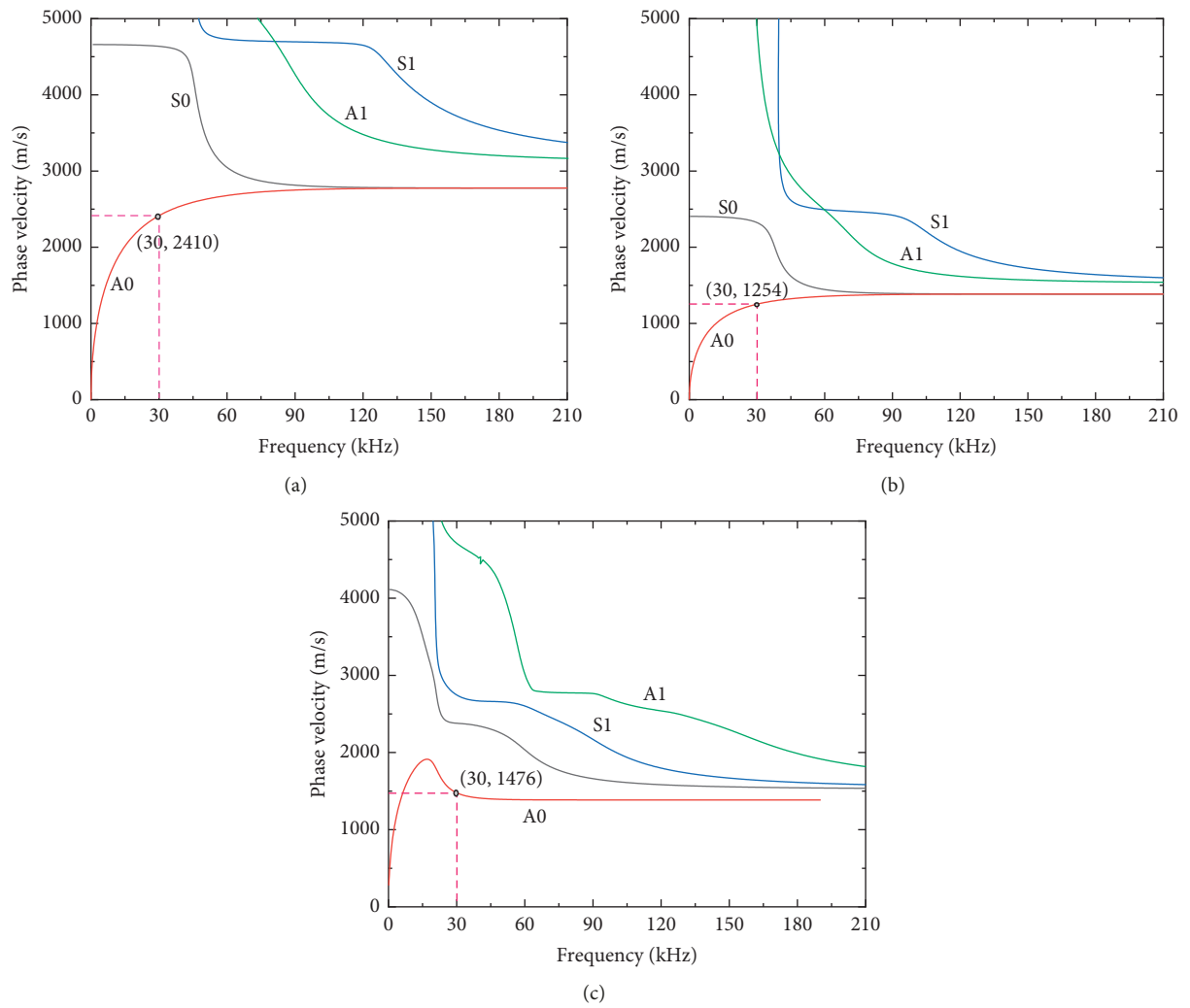


FIGURE 4: Phase velocity dispersion curves: (a) the first layer; (b) the second layer; (c) two layers.

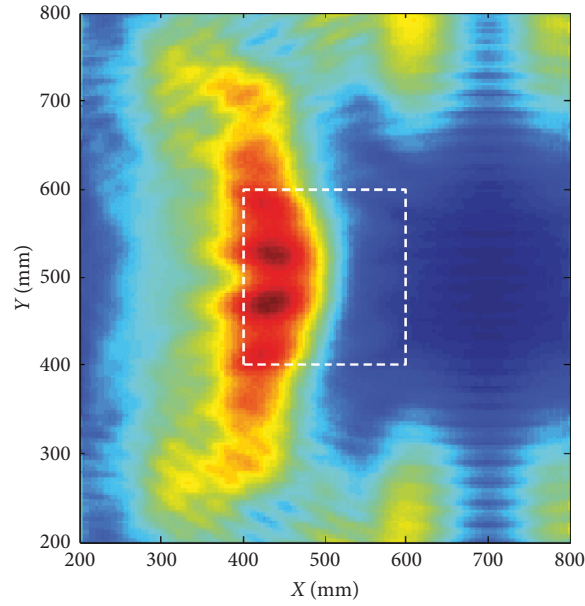
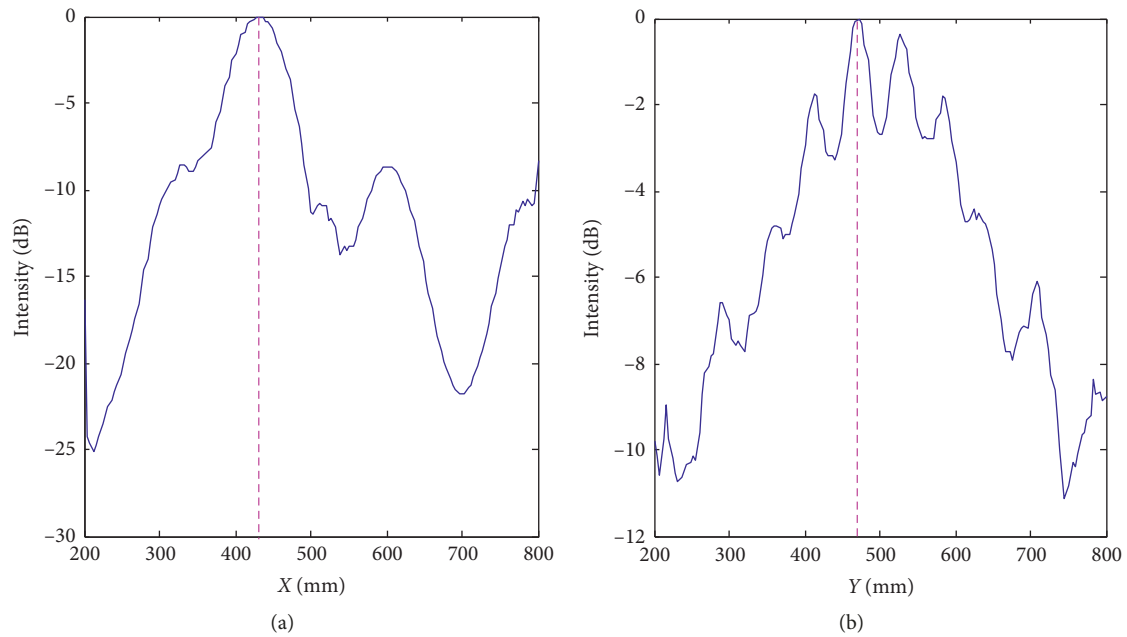


FIGURE 5: SAFT imaging results (finite element simulation).

FIGURE 6: SAFT imaging intensity profile in (a) the X direction of the point (432 mm, 471 mm) and (b) the Y direction of the point (432 mm, 471 mm).

The five-period sinusoidal pulse with the Hanning window is used as an excitation signal with a central frequency of 30 kHz. The time-domain waveform and spectrum of the excitation signal are shown in Figure 3.

Figure 4 shows the phase velocity dispersion curves obtained by a commercial software package called Disperse (version 2.0.20a, Imperial College London, UK). Figure 4(a) shows the phase velocity dispersion curves in the first layer. The phase velocity of the A0 mode is 2410 m/s when the frequency is 30 kHz. Therefore, the wavelength is 78.2 mm. The relationship between the defect size and the wavelength

is $d/\lambda \approx 2.56$. Figure 4(b) shows the phase velocity dispersion curves in the second layer. The phase velocity of the A0 mode is 1254 m/s when the frequency is 30 kHz. Therefore, the wavelength is 150.3 mm. The relationship between the defect size and the wavelength is $d/\lambda \approx 1.33$. Figure 4(c) shows the phase velocity dispersion curves in two layers. The phase velocity of the A0 mode is 1476 m/s when the frequency is 30 kHz. Therefore, the wavelength is 49.2 mm. The relationship between the defect size and the wavelength is $d/\lambda \approx 1.57$. Obviously, the phase velocity dispersion curves are strikingly different in the multilayer structure and the single-

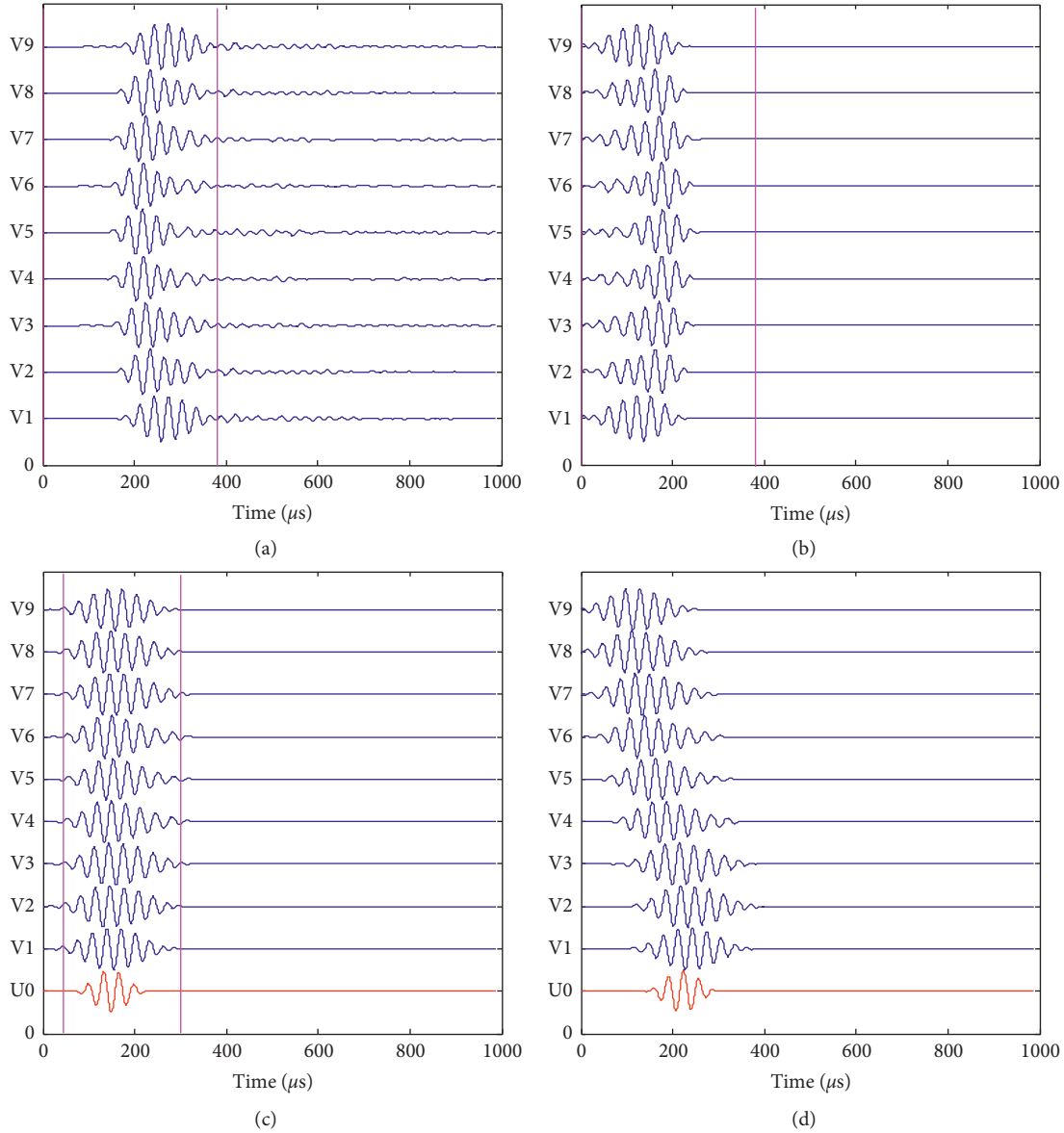


FIGURE 7: Focusing of the direct and adjoint sound fields at the defect: (a) scattered signals received by all receiving sensors; (b) scattered signal after time reversal; (c) scattered signals reaching the defect; (d) scattered signals reaching the nondefective point.

layer structure. Therefore, we have to take this difference into consideration in order to improve the test results of a cavity defect which is located at the interface between the first layer and the second layer.

The signal acquisition process is as follows: the excitation probe is placed at S1, the receiving probe moves from R1 to R9, and nine groups of experimental signals are collected successively [31]. After signal collection at nine positions is completed, the excitation probe is moved to S2, the receiving probe moves from R1 to R9, and nine groups of experimental signals are collected. By analogy, 9×9 groups of experimental signals were collected.

The finite element simulation data were used to conduct SAFT imaging, and the imaging results are shown in Figure 5. The dotted frame in the imaging figure was the cavity area. In the SAFT imaging intensity profile in Figure 6,

the intensity peak in the X direction is at $X = 432$ mm, and the intensity peak in the Y direction is at $Y = 471$ mm. Therefore, the center position of the cavity defect represented by the SAFT imaging method is (432 mm, 471 mm). The measured position (432 mm, 471 mm) is represented by (x_{d1}, y_{d1}) , and the center position of the actual cavity defect (500 mm, 500 mm) is represented by (x_{d2}, y_{d2}) . The positioning error of the cavity defect is defined as E , and $E = 74$ mm is obtained.

Taking the excitation source S5 whose coordinate position is (300 mm, 500 mm) as an example, the focusing process of the direct and the adjoint sound fields at the defect in topological imaging is described [32]. As shown in Figure 7, V1–V9 are the scattered signals, and U0 is the direct sound field signal. Figure 7(a) is the scattering signal received by all the receiving sensors. Figure 7(b) shows the

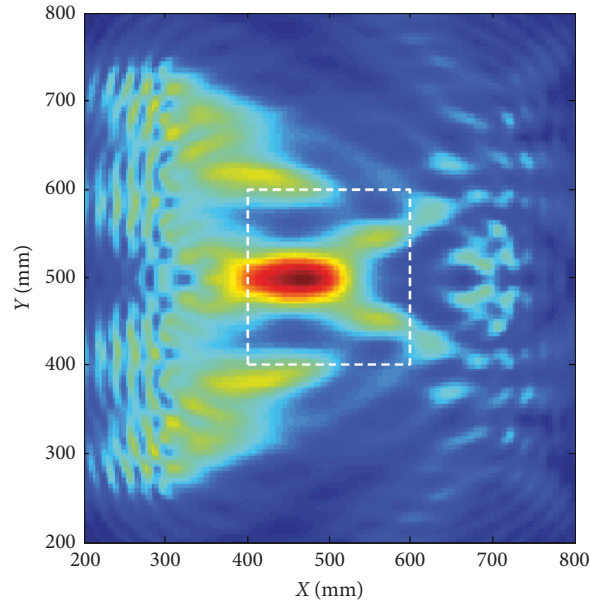
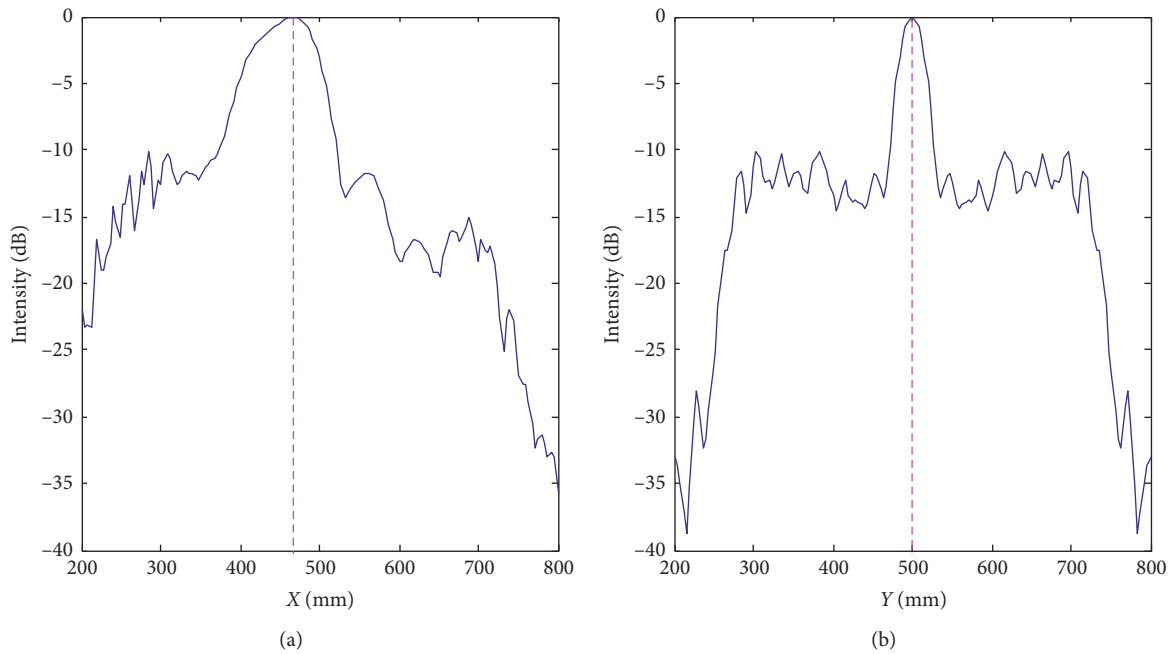


FIGURE 8: TDTE imaging results (finite element simulation).

FIGURE 9: TDTE imaging intensity profile in (a) the X direction of the point (470 mm, 500 mm) and (b) the Y direction of the point (470 mm, 500 mm).

time reversal of scattered signals received by all the receiving sensors in the time window (0–396.3 μ s). Figure 7(c) is the scattered signal reaching the defect. Figure 7(d) is the scattered signal reaching the nondefective point. By comparing Figures 7(c) and 7(d), it is clear that the scattered signal is focused at the defect, whereas the scattered signal reaching the nondefective area is not focused.

On the basis of focusing scattered signals, equation (4) is used to calculate the topological energy value in the time domain, which is taken as the imaging function. The imaging

results are shown in Figure 8. In the time-domain topological energy imaging intensity profile in Figure 9, the intensity peak in the X direction is at $X=470$ mm, and the intensity peak in the Y direction is at $Y=500$ mm. Therefore, the center position of the cavity defect represented by topological energy imaging in the time domain is (470 mm, 500 mm), and the positioning error with the center position of the actual cavity defect (500 mm, 500 mm) is $E=30$ mm.

In terms of positioning accuracy, the TDTE imaging can realize a more accurate positioning of the cavity defect than

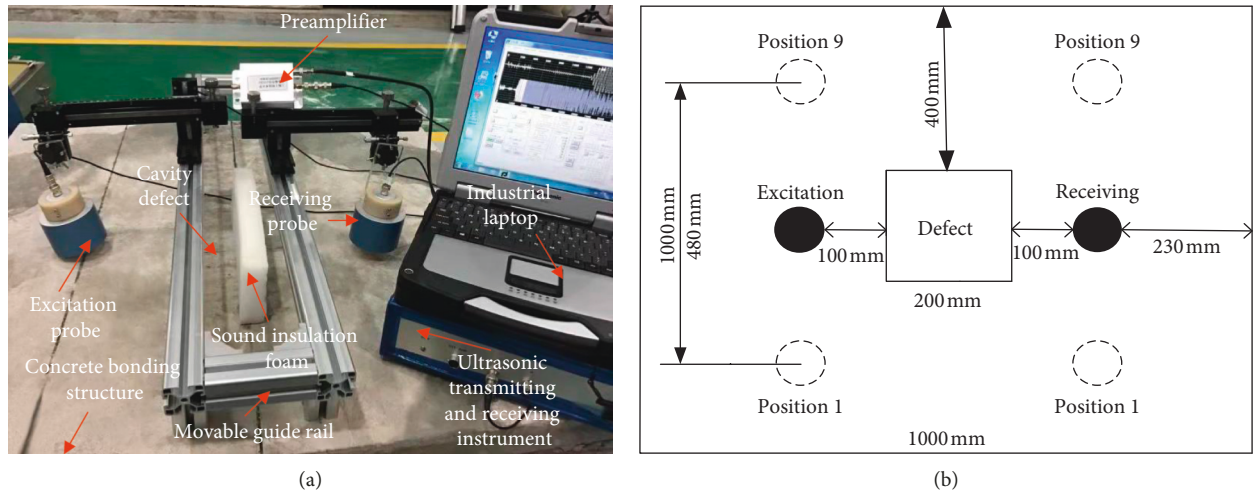


FIGURE 10: (a) Experimental system and (b) schematic of the signal acquisition mode.

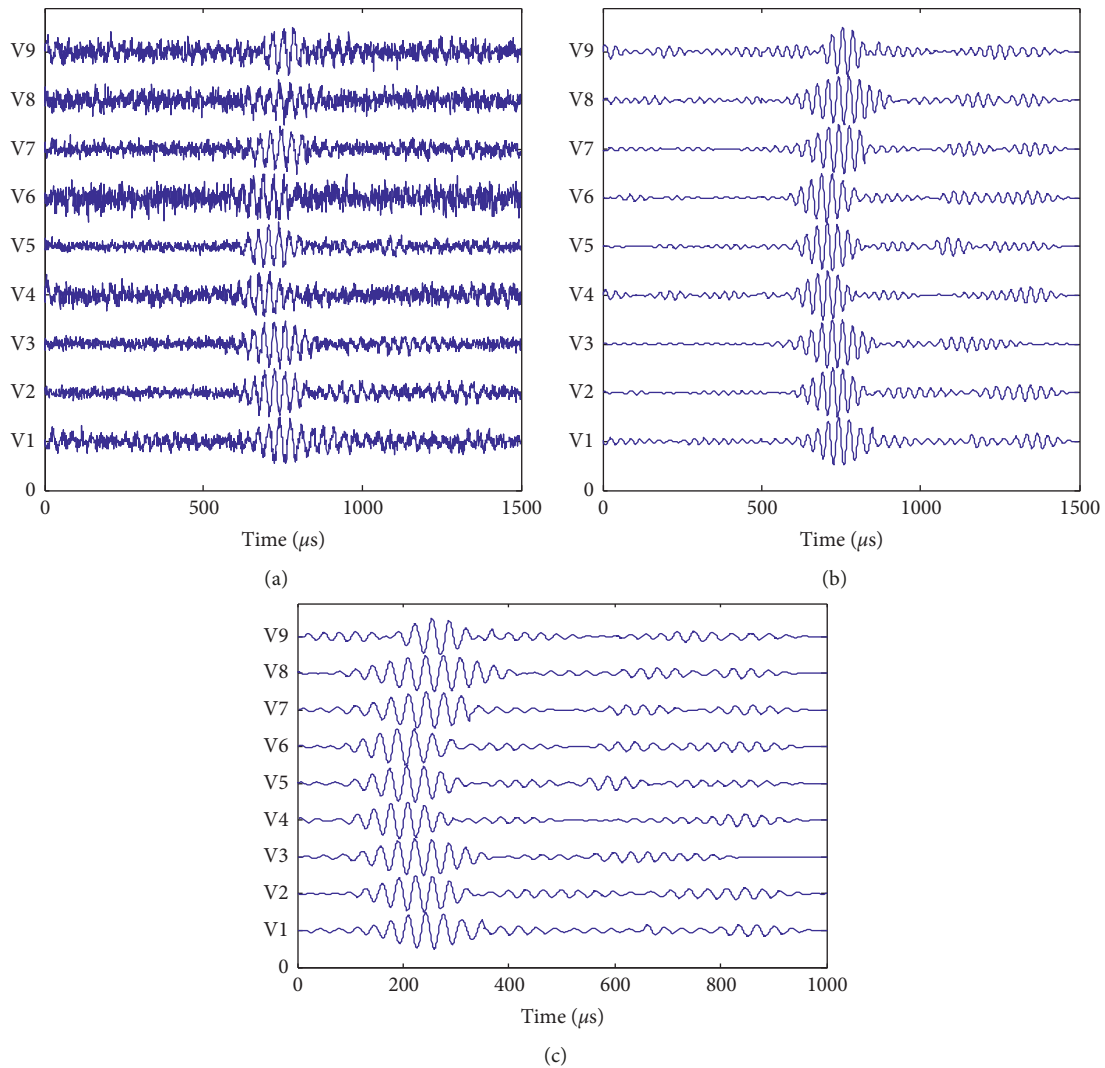


FIGURE 11: Original and preprocessed scattering signals obtained at S5 position of the excitation source: (a) original scattering signal; (b) filtered scattering signal; (c) scattering signal after calibration.

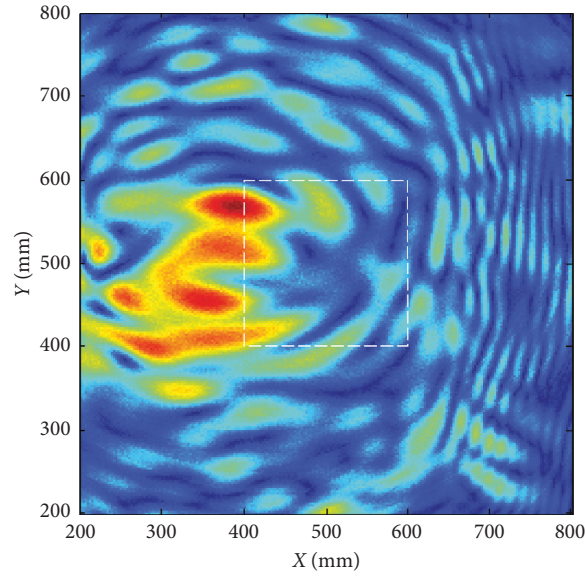
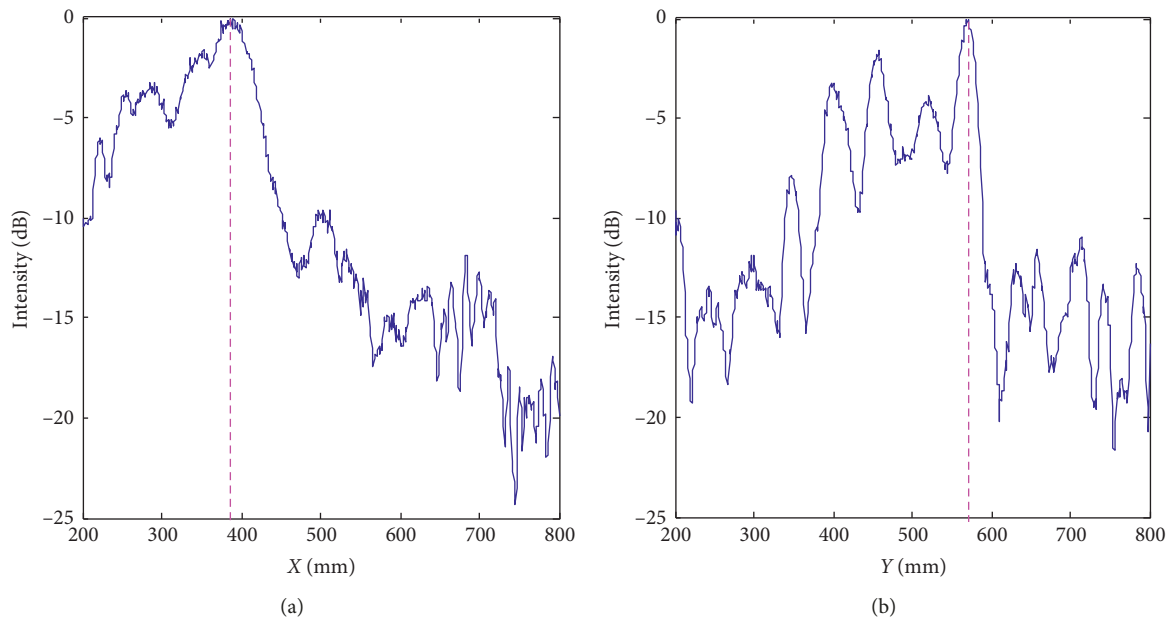


FIGURE 12: SAFT imaging experimental results.

FIGURE 13: SAFT imaging intensity profile in (a) the X direction of the point (388 mm, 572 mm) and (b) the Y direction of the point (388 mm, 572 mm).

the SAFT imaging method which can only determine the approximate location of the defect. In terms of representing the region and artifact distribution of the cavity defect, the defect region represented by topological energy imaging in the time domain is relatively concentrated with few artifacts, whereas the defect region represented by SAFT imaging has a large range with additional artifacts.

4. Experimental Research

The experimental system is shown in Figure 10(a). The data acquisition method of the experimental signals is consistent with that of finite element simulation, as shown in

Figure 10(b). JPR-600C, developed by Japan Probe Corporation, is used as the ultrasonic transmitting and receiving instrument. The excitation voltage is 550 V, the carrier frequency is 30 kHz, the number of pulses is 6, the repetition frequency is 100 Hz, and the sampling rate is 1 Mbit/s. Air-coupled ultrasonic probes with a center frequency of 30 kHz are tilted by 8.2° . A sponge is attached to the surface of the plate-like structure between the transmitting and receiving probes to reduce the effect of noise in the air. To improve the SNR, the experimental signals were averaged for 64 times. In addition, the level calibration of the concrete bonded structure was carried out before the experiment.

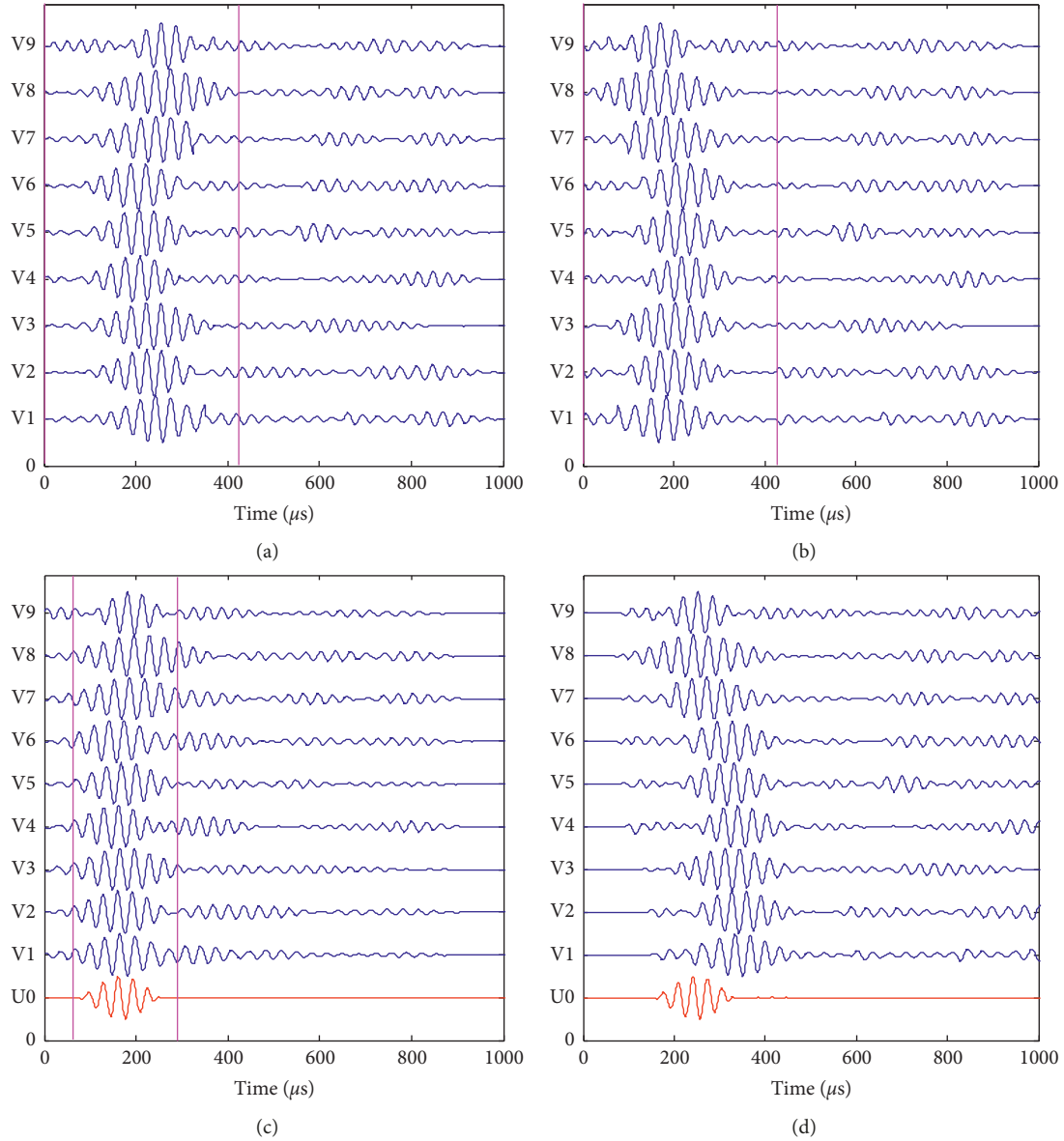


FIGURE 14: Focusing of the direct and adjoint sound fields at the defect: (a) scattered signals received by all receiving sensors; (b) scattered signals after time reversal; (c) scattered signal reaching the defect; (d) scattered signal reaching the nondefective point.

Taking the excitation source S5 with coordinate position (300 mm, 500 mm) as an example, the scattering signal obtained in the experiment and the preprocessed scattering signal such as filtering and calibration are shown in Figure 11.

The preprocessed experimental signals were imaged by SAFT imaging, and the imaging results are shown in Figure 12. In the SAFT imaging intensity profile in Figure 13, the intensity peak in the X direction is at $X=388$ mm, and the intensity peak in the Y direction is at $Y=572$ mm. The center position of the cavity defect represented by the SAFT imaging method was (388 mm, 572 mm), and the positioning error with the actual center position of the cavity defect (500 mm, 500 mm) was $E=142$ mm.

Taking the excitation source S5 whose coordinate position is (300 mm, 500 mm) as an example, the focusing

process of the direct sound field and the adjoint sound field at the defect in topological imaging is described. As shown in Figure 14, V1–V9 are the scattered signals and U0 is the direct sound field signal. Figure 14(a) is the scattering signal received by all the receiving sensors. Figure 14(b) shows the time reversal of scattered signals received by all the receiving sensors in the time window (0–424 μ s). Figure 14(c) is the scattered signal reaching the defect. Figure 14(d) is the scattered signal reaching the nondefective point. By comparing Figures 14(c) and 14(d), it is clear that the scattered signal is focused at the defect and not at the nondefective area.

Topological energy imaging results in the time domain are shown in Figure 15. According to the time-domain topological energy imaging intensity profile in Figure 16, the intensity peak in the X direction is at $X=468$ mm, and the

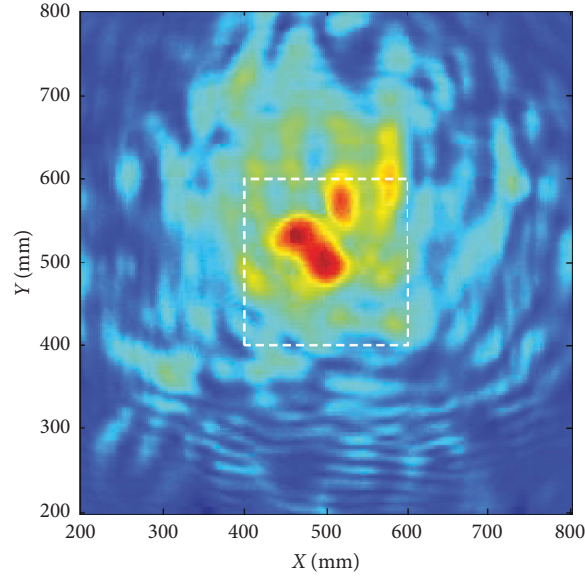


FIGURE 15: TDTE imaging experimental results.

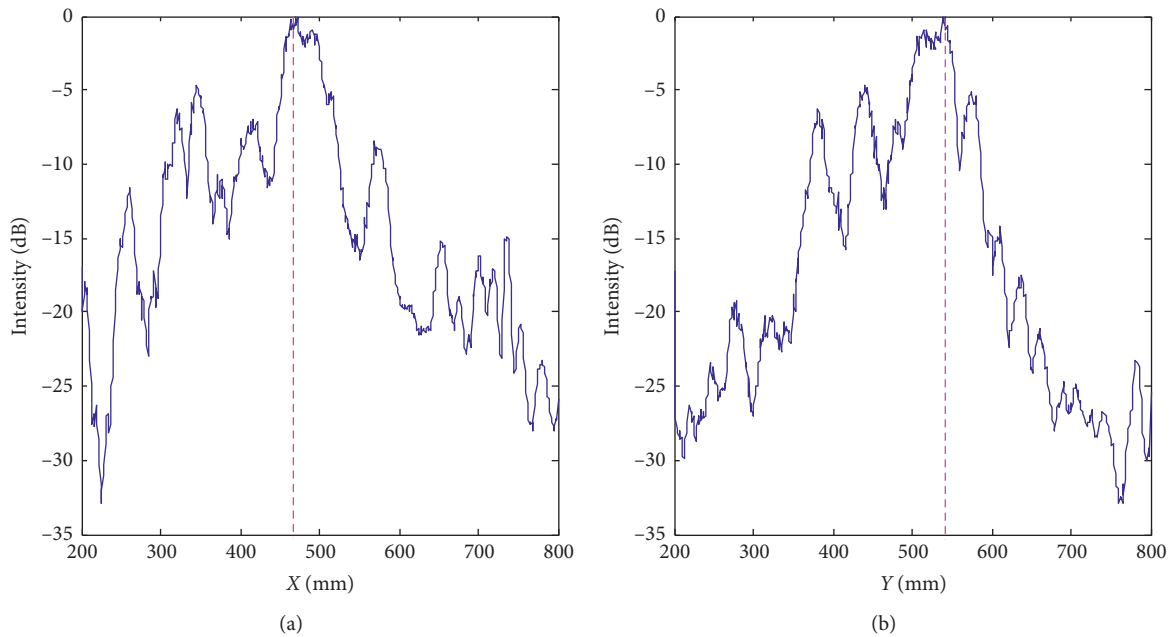


FIGURE 16: TDTE imaging intensity profile in (a) the X direction of the point (468 mm, 552 mm) and (b) Y direction of the point (468 mm, 552 mm).

intensity peak in the Y direction is at $Y = 552$ mm. The center position of the cavity defect in the topological energy imaging in the time domain is (468 mm, 552 mm), and the positioning error between the center position of the actual cavity defect (500 mm, 500 mm) is $E = 61$ mm.

The experimental results are consistent with the finite element results. The TDTE method can achieve a more accurate location of the cavity defects, and the defect areas characterized by energy imaging are relatively concentrated, with fewer artifacts, than the SAFT method.

5. Conclusion

In this study, an ultrasonic Lamb wave high-precision imaging method for realizing multilayer concrete cavity defects using TDTE is proposed. The method is based on the calculation of direct and adjoint sound fields in the defect-free reference medium, and the excitation signal of the sensor is used as the source calculation. Then, in the sound field, the Lamb wave scattering signal caused by the cavity defect is used as the sound source to calculate the adjoint sound field.

Finally, the direct sound field is multiplied by the adjoint sound field to obtain the time-domain topological energy value as the imaged pixel value. The TDTE method is much better for multilayer structure as it is based on the focusing effect of the forward acoustic field and the adjoint acoustic field. More specifically, the forward acoustic field and the adjoint acoustic field will only be focused at the defect's position. Therefore this method can improve the positioning accuracy of the imaging system and reduces artifacts. On the basis of numerical simulations and experimental results, and compared with the results of the SAFT method, the following conclusions are drawn:

- (i) Using the time reversal method, the direct sound field and the accompanying sound field can be focused at the defect instead of the defect-free area. By multiplying the direct sound field and the adjoint sound field, the interference of multimode aliasing at the defect-free point can be eliminated. Therefore the TDTE imaging has the higher positioning accuracy and fewer artifacts than the SAFT method.
- (ii) The numerical simulation and experimental results show that the location accuracy of TDTE imaging is higher than that of traditional SAFT.
- (iii) The numerical simulation and experimental results show that the artifacts in the TDTE imaging results are significantly less than those in the traditional SAFT method.

Data Availability

The data used to support the findings of this study are available from the corresponding author upon request.

Disclosure

The funders had no role in the design of the study; in the collection, analyses, or interpretation of data; and in the writing of the manuscript; or in the decision to publish the results.

Conflicts of Interest

The authors declare that they have no conflicts of interest.

Acknowledgments

The authors thank the National Natural Science Foundation of China (nos. 51975347, 11674214, and 51907117). The authors also thank the Key Science and Technology Support Project of Shanghai Science and Technology Commission (no. 18030501300). The present study was conducted on the basis of the frameworks of the mentioned research.

References

- [1] N. M. Zahari, A. Madun, S. H. Dahlan et al., "Experimental detection and characterization of void using time domain reflection wave," *Journal of Physics: Conference Series*, vol. 995, Article ID 012102, 2018.
- [2] C. Cheng and Z. Shen, "Time-series based thermography on concrete block void detection," in *Proceedings of the Construction Research Congress 2018*, New Orleans, LA, USA, April 2018.
- [3] S. B. Zheng, Q. W. Zhong, X. D. Chai, X. Chen, and L. Peng, "A novel prediction model for car body vibration acceleration based on correlation analysis and neural networks," *Journal of Advanced Transportation*, vol. 2018, Article ID 1752070, 13 pages, 2018.
- [4] M. S. Khan, G. A. Washer, and S. B. Chase, "Evaluation of dual-band infrared thermography system for bridge deck delamination surveys," in *Proceedings of the Structural Materials Technology III: An NDT Conference*, San Antonio, TX, USA, March 1998.
- [5] J. S. Popovics, J. R. Roesler, J. Bittner et al., *Ultrasonic Imaging for Concrete Infrastructure Condition Assessment and Quality Assurance*, Illinois Department of Transportation, Springfield, IL, USA, 2017.
- [6] J. Krieger, M. Krause, and H. Wiggenger, "Tests and assessments of NDT methods for concrete bridges," in *Proceedings of SPIE—Structural Materials Technology III: An NDT Conference*, San Antonio, TX, USA, March 1998.
- [7] K. Fukuyama, Y. Higashibata, and Y. Miyauchi, "Studies on repair and strengthening methods of damaged reinforced concrete columns," *Cement and Concrete Composites*, vol. 22, no. 1, pp. 81–88, 2000.
- [8] L. Khazanovich, R. Velasquez, and E. G. Nesvijski, "Evaluation of top-down cracks in asphalt pavements by using a self-calibrating ultrasonic technique," *Transportation Research Record: Journal of the Transportation Research Board*, vol. 1940, pp. 63–68, 2005.
- [9] K. Hoegh, L. Khazanovich, K. Maser, and N. Tran, "Evaluation of ultrasonic technique for detecting delamination in asphalt pavements," *Transportation Research Record: Journal of the Transportation Research Board*, vol. 2306, no. 1, pp. 105–110, 2012.
- [10] I.-M. Lee, Q. Hung Truong, D.-H. Kim, and J.-S. Lee, "Discontinuity detection ahead of a tunnel face utilizing ultrasonic reflection: laboratory scale application," *Tunneling and Underground Space Technology*, vol. 24, no. 2, pp. 155–163, 2009.
- [11] A. O. De La Haza, A. A. Samokrutov, and P. A. Samokrutov, "Assessment of concrete structures using the Mira and Eyecon ultrasonic shear wave devices and the SAFT-C image reconstruction technique," *Construction and Building Materials*, vol. 38, pp. 1276–1291, 2013.
- [12] H. Wu, J. Chen, K. Yang, and X. Hu, "Ultrasonic array imaging of multi-layer structures using full matrix capture and extended phase shift migration," *Measurement Science and Technology*, vol. 27, no. 4, Article ID 045401, 2016.
- [13] D. Connolly, A. Giannopoulos, W. Fan, P. K. Woodward, and M. C. Forde, "Optimising low acoustic impedance back-fill material wave barrier dimensions to shield structures from ground borne high speed rail vibrations," *Construction and Building Materials*, vol. 44, pp. 557–564, 2013.
- [14] W. F. Zhu, X. J. Chen, Z. W. Li et al., "A SAFT method for the detection of void defect inside a ballastless track structure using ultrasonic array sensors," *Sensors*, vol. 19, no. 21, p. 4677, 2019.
- [15] K. Qin, C. Yang, and F. Sun, "Generalized frequency-domain synthetic aperture focusing technique for ultrasonic imaging of irregularly layered objects," *IEEE Transactions on Ultrasonics, Ferroelectrics, and Frequency Control*, vol. 61, no. 1, pp. 133–146, 2014.

- [16] M. H. Skjelvareid, T. Olofsson, Y. Birkelund, and Y. Larsen, "Synthetic aperture focusing of ultrasonic data from multi-layered media using an omega-K algorithm," *IEEE Transactions on Ultrasonics, Ferroelectrics and Frequency Control*, vol. 58, no. 5, pp. 1037–1048, 2011.
- [17] T. Scharrer, A. Koch, K. T. Fendt et al., "Ultrasonic defect detection in multi-material, axis-symmetric devices with an improved synthetic aperture focusing technique (SAFT)," in *Proceedings of the 2012 IEEE Ultrasonics Symposium*, Dresden, Germany, October 2012.
- [18] G. Fan, H. Zhang, W. Zhu, H. Zhang, and X. Chai, "Numerical and experimental research on identifying a delamination in ballastless slab track," *Materials*, vol. 12, no. 11, p. 1788, 2019.
- [19] M. S. Harb and F. G. Yuan, "Lamb wave dispersion and anisotropy profiling of composite plates via non-contact air-coupled and laser ultrasound," *AIP Conference Proceedings*, vol. 1229, p. 1650, 2015.
- [20] M. S. Harb and F. G. Yuan, "Non-contact ultrasonic technique for Lamb wave characterization in composite plates," *Ultrasonics*, vol. 64, pp. 162–169, 2016.
- [21] K. Xu, J.-G. Minonzio, D. Ta, B. Hu, W. Wang, and P. Laugier, "Sparse SVD method for high-resolution extraction of the dispersion curves of ultrasonic guided waves," *IEEE Transactions on Ultrasonics, Ferroelectrics, and Frequency Control*, vol. 63, no. 10, pp. 1514–1524, 2016.
- [22] Z. L. Liu, X. Zhong, T. Dong, C. He, and B. Wu, "Delamination detection in composite plates by synthesizing time-reversed Lamb waves and a modified damage imaging algorithm based on RAPID," *Structural Control and Health Monitoring*, vol. 24, no. 5, Article ID e1919, 2017.
- [23] Y. L. He, J. K. Shen, Z. W. Li, and H.-Y. Lu, "Fractal characteristics of transverse crack propagation on CRTSII type track slab," *Mathematical Problems in Engineering*, vol. 2019, Article ID 6587343, 9 pages, 2019.
- [24] H. Zhang, H. Zhang, J. Zhang et al., "Wavenumber imaging of near-surface defects in rails using Green's function reconstruction of ultrasonic diffuse fields," *Sensors*, vol. 19, no. 17, p. 3744, 2019.
- [25] H. Zhang, H. Y. Zhang, M. Y. Xu, G. P. Fan, W. F. Zhu, and X. D. Chai, "Lamb waves topological imaging combining with Green's function retrieval theory to detect near filed defects in isotropic plates," *Chinese Physics B*, vol. 28, no. 7, Article ID 074301, 2019.
- [26] M. Bonnet and B. B. Guzina, "Sounding of finite solid bodies by way of topological derivative," *International Journal for Numerical Methods in Engineering*, vol. 61, no. 13, pp. 2344–2373, 2004.
- [27] C. Zhang, S. G. Yan, B. X. Zhang, and W.-h. Lv, "Topological imaging in layered plate by guided waves," in *Proceedings of the 2016 Symposium on Piezoelectricity, Acoustic Waves, and Device Applications (SPAWDA)*, Xi'an, China, October 2016.
- [28] K. Suenaga, H. Wakabayashi, M. Koshino, Y. Sato, K. Urita, and S. Iijima, "Imaging active topological defects in carbon nanotubes," *Nature Nanotechnology*, vol. 2, no. 6, pp. 358–360, 2007.
- [29] S. Rodriguez, M. Deschamps, M. Castaings, and E. Ducasse, "Guided wave topological imaging of isotropic plates," *Ultrasonics*, vol. 54, no. 7, pp. 1880–1890, 2014.
- [30] E. Lubeigt, S. Mensah, S. Rakotonarivo, J.-F. Chaix, F. Baqué, and G. Gobillot, "Topological imaging in bounded elastic media," *Ultrasonics*, vol. 76, pp. 145–153, 2017.
- [31] M. Yuan, Z. Cao, J. Luo, and X. Chou, "Recent developments of acoustic energy harvesting: a review," *Micromachines*, vol. 10, no. 1, p. 48, 2019.
- [32] F. Y. Ma, J. Y. Chen, and J. H. Wu, "Three-dimensional acoustic sub-diffraction focusing by coiled metamaterials with strong absorption," *Journal of Materials Chemistry C*, vol. 7, no. 17, pp. 5131–5138, 2019.

